metals

MDPI

Article

Theoretical Predictions of Structure, Mechanics, Dislocation, and Electronics Properties of FeTi Alloy at High Pressure

Linkun Zhang [1], Hong Chen [1], Zhipeng Wang [2,*], Li Ma [3] and Pingying Tang [3]

[1] College of Materials Science and Engineering, Central South University of Forestry and Technology, Changsha 410004, China
[2] State Key Laboratory of Advanced Design and Manufacturing for Vehicle Body, Hunan University, Changsha 410082, China
[3] Key Laboratory of New Electric Functional Materials, Guangxi College, Nanning Normal University, Nanning 530023, China
* Correspondence: wangzp1205@163.com

Abstract: The influences of applied pressure on the structure, mechanics, dislocation, and electronics properties of an FeTi hydrogen storage alloy are theoretically investigated via first-principles calculations. The lattice parameter ratio, elastic constant, Young's modulus, bulk modulus, shear modulus, ductile/brittle, Poisson's ratio, anisotropy, Cauchy pressure, yield strength, Vickers hardness and energy factor are discussed versus applied pressure. The results show that the FeTi alloy exhibits good mechanical stability under applied pressure between 0 and 50 GPa, and the mechanical properties are significantly improved under applied pressure, like the resistances to elastic, bulk, and shear deformations, the material ductility and metallicity, as well as Vickers hardness and yield strength. Moreover, the electronic structures reveal that the FeTi alloy has metallic properties and the structural stability of the FeTi hydrogen storage alloy is enhanced at high pressure. This work provides significant value for high-pressure applications of FeTi alloys in hydrogen storage and supply fields.

Keywords: FeTi alloy; hydrogen storage; density functional theory; mechanical properties; energy factor; high pressure

check for updates

Citation: Zhang, L.; Chen, H.; Wang, Z.; Ma, L.; Tang, P. Theoretical Predictions of Structure, Mechanics, Dislocation, and Electronics Properties of FeTi Alloy at High Pressure. *Metals* **2023**, *13*, 1547. https://doi.org/10.3390/met13091547

Academic Editor: Shahram Solaymani

Received: 30 June 2023
Revised: 29 August 2023
Accepted: 31 August 2023
Published: 1 September 2023

Copyright: © 2023 by the authors. Licensee MDPI, Basel, Switzerland. This article is an open access article distributed under the terms and conditions of the Creative Commons Attribution (CC BY) license (https://creativecommons.org/licenses/by/4.0/).

1. Introduction

The increasing demand for energy and the use of fossil fuels have potential threats to society. Therefore, it is becoming more and more important to find an alternative to fossil fuels. Hydrogen is considered as a benign and promising energy vector [1–3]. Nonetheless, how to store hydrogen efficiently and economically is an urgent problem to be solved. In the search for suitable hydrogen storage materials, many researchers pay attention to FeTi alloys. FeTi alloys will be an excellent candidate for hydrogen storage due to their cheap price and ability to store hydrogen under mild pressure and at room temperature [4,5]. In addition, FeTi alloys have gained widespread application in a variety of industries due to their low density, high strength, and excellent biocompatibility [6], and they have gradually become a research hotspot.

Up to now, FeTi alloys have been widely studied by researchers in terms of hydrogen storage, and many research results have been obtained through theory and experiments [7–11]. Padhee et al. [12] studied the relation of Mn addition in FeTi alloys and hydrogen storage capacity. They adopted density functional theory (DFT) calculations to explore the thermodynamic and kinetic properties of hydrogen absorption in unprocessed and doped FeTi, and the experiment results revealed that Mn addition was beneficial to the retention of hydrogen capacity, which is conducive to the practical application of FeTi alloys. Based on the Open Calphad software (https://www.opencalphad.com/, accessed on 28 August 2023), Alvares et al. [13] explored the same properties for $FeTi_{1-x}H_x$ ($0 \leq x \leq 1$) alloys and

acquired new thermodynamic data via first-principles calculations, which facilitated the subsequent study of new-type FeTi-based hydrides. Nong et al. [14] probed the relevant mechanical parameters of FeTi alloys by first-principles calculations, as well as hydrogen diffusion behavior, and the same method was applied to calculate the activation energy of hydrogen diffusion within octahedron interstices, and the calculated activation energy was 2.92 eV. Benyelloul et al. [15] successfully obtained elastic constants of FeTi intermetallic via the stress–strain curve and calculated the shear modulus, Young's modulus, anisotropic factors, and Poisson's ratio. The results indicated that a high hydrogen concentration increased the ductility of FeTi compounds by analyzing the B/G ratio. In addition, Zhu et al. [16] calculated the thermodynamic and other relevant parameters of equiatomic FeTi alloys via the DFT method, and the electronic structure was particularly stable under hydrostatic pressure, which agreed well with the available data.

Based on previous studies, a large number of experiments and theories have proved the many excellent properties of FeTi hydrogen storage alloys. However, to date, no prior research has been conducted on the structure, mechanics, dislocation, and electronics properties of FeTi hydrogen storage alloys under high pressure. In this study, we conduct a comprehensive investigation into the structure, mechanics, dislocation, and electronics properties of FeTi alloys at high pressure. Our study involves calculating various parameters, including the dimensionless volume ratio, elastic constants, Young's modulus, shear modulus, bulk modulus, Poisson's ratio, anisotropy, ductile/brittle, and electronic properties. The results demonstrate excellent agreement with both experimental and theoretical findings, producing significant implications for the design and application of FeTi alloys in hydrogen storage and other industrial sectors.

2. Methodology

In this work, the Vienna ab initio simulation package [17,18] was adopted for performing all energy calculations. The projector augmented-wave method [19] was utilized to handle ion–electron interactions. According to the definition of Perdew et al. [20], the generalized-gradient approximation of Perdew–Burke–Eruzerhof was adopted for the exchange–correlation functional. Valance electrons of Fe and Ti atoms were denoted as Fe ($3d^6 4s^2$) and Ti ($3d^2 4s^2$). To obtain sufficient convergent computational parameters, we conducted rigorous convergence tests before structural optimization. For the FeTi alloy, the cutoff energy and gamma-centered Monkhorst–Pack grids of k-mesh were 500 eV and $10 \times 10 \times 10$ after optimization [21]. During calculations, the elastic constant C_{ij} and strain-stress relationship were calculated using the finite difference method. The pressure changed from 0 to 50 GPa. The convergence criterion for self-consistent calculation satisfied the condition that the Hellmann–Feyman force is lower than 0.01 eV/Å, and the energy criterion converged to 10^{-6} eV/atom. Figure 1 describes the cubic crystal structure of an FeTi unit cell, and the space group belongs to *Pm*-3*m*.

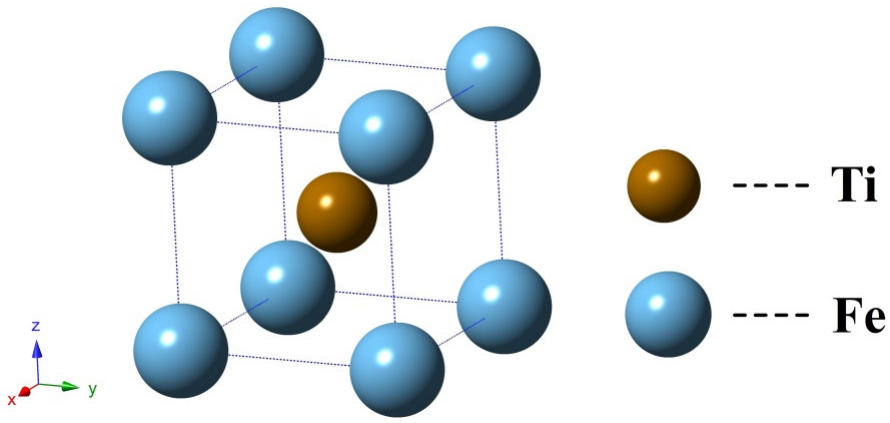


Figure 1. Cubic structure of FeTi unit cell with $a_0 = 2.945$ Å.

3. Results and Discussions

3.1. Structure Properties and Stability

To determine the steady-state structure of the FeTi alloy, the Birch–Murnaghan equation of state (EOS) [22] was used to fit the relationships between the total energy and volume V of the primitive cell, V is between 0.9 V_0 and 1.1 V_0. The unit cell is fully optimized for calculating the total energy in the ground state. As depicted in Figure 2, the minimum total energy is $E_t = -16.8347$ eV at $V = V_0$ ($V_0 = 25.55$ Å^3), where the lattice parameter is $a_0 = 2.945$ Å, and a_0 is defined as optimized lattice parameter under $P = 0$ and $T = 0$. The obtained calculations are consistent with experimental [23,24] and theoretical findings [5,14–16,25], as detailed in Table 1.

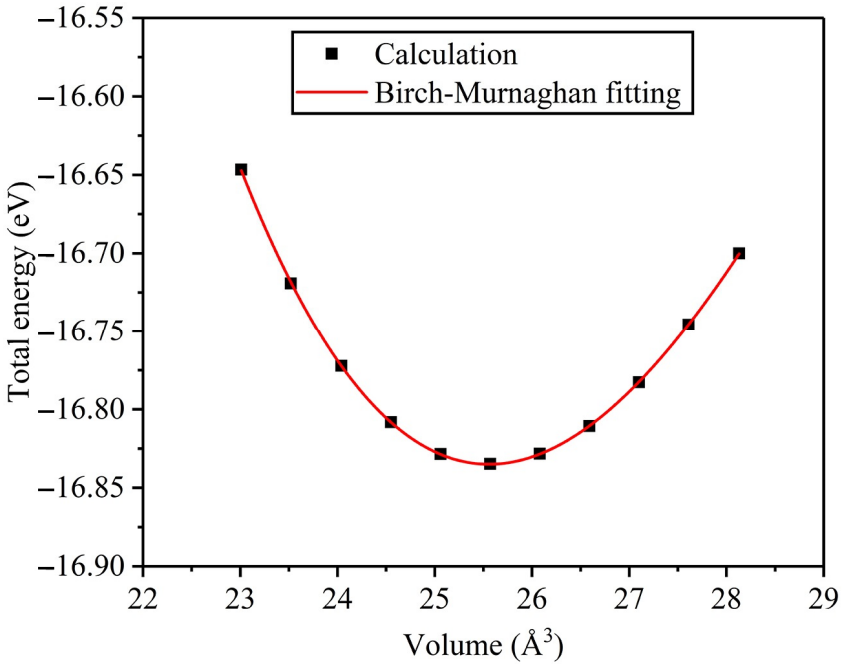


Figure 2. The fitted relationships between total energy and volume of primitive cell.

Table 1. Lattice parameter compared to experimental and theoretical data for FeTi alloy.

FeTi	Present	Experiments	Theoretical Data
Lattice parameter	2.945	2.978 [23], 2.972 [24]	2.943 [15], 2.953 [14], 2.95 [16] 2.96 [5], 2.97 [25]

To analyze the influence of applied pressure on the cell volume and lattice parameter of the FeTi alloy, some structure optimizations were carried out to calculate the equilibrium lattice parameter at multiple pressures. The V/V_0 and a/a_0 ratios of cell volume and lattice parameter are shown in Figure 3 with regard to applied pressure. Figure 3 shows that the V/V_0 and a/a_0 ratios decrease with an increase in applied pressure, and the V/V_0 ratio of volume compression under pressure is much smaller than the a/a_0 ratio of lattice parameter compression, indicating that the inter-atomic distance becomes smaller and the electronic interaction is enhanced under high pressure.

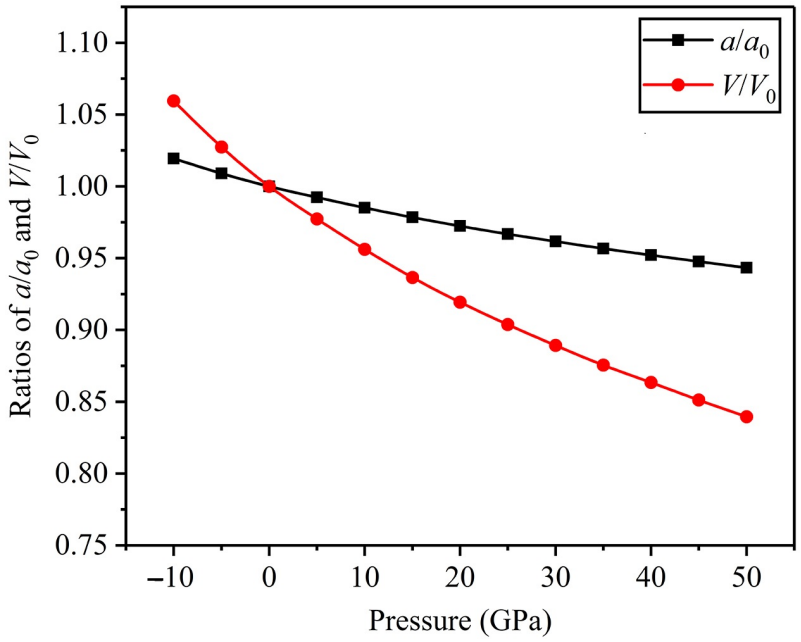


Figure 3. Relation curves of V/V_0 and a/a_0 ratios versus applied pressure.

For anisotropic materials, the structural stability of materials depends on elastic constants C_{ij}, reflecting the ability to resist stress. For cubic crystals, elastic constants C_{ij} include C_{11}, C_{12}, and C_{44}. According to the stability criterion of cubic structures [26–28], C_{11}, C_{12}, and C_{44} must meet the general expressions:

$$(C_{11} - C_{12}) > 0,\ C_{11} > 0,\ C_{44} > 0,\ (C_{11} + 2C_{12}) > 0 \quad (1)$$

As presented in Table 2, we write down the above parameters under $P = 0$ and $T = 0$, including Young's modulus E, bulk modulus B, shear modulus G, and Poisson's ratio σ. In comparison, the results of this work consist with experiments [29,30] and theoretical calculations [14–16,31].

Table 2. Calculated results compared to other experiments and theoretical calculations under $T = 0$ and $P = 0$ (Unit: GPa).

FeTi	Present	Experiments	Theoretical Calculations
C_{11}	379.44	310 [30], 325 [29]	304 [31], 351.70 [14], 384.74 [15], 385 [16]
C_{12}	100.89	86.2 [30], 121 [29]	136 [31], 86.82 [14], 102.42 [15], 95 [16]
C_{44}	71.04	74.9 [30], 69 [29]	138 [31], 73.08 [14], 66.96 [15], 72 [16]
B	193.74	160.8 [30], 189 [29]	175.11 [14], 196.52 [15], 191.66 [16]
E	241.28	223 [30], 213 [29]	236.88 [14], 235.84 [15], 244.58 [16]
G	93.34	88 [30], 81 [29]	92.93 [14], 90.71 [15], 95 [16]
σ	0.21	0.26 [30], 0.31 [29]	0.27 [14], 0.29 [15], 0.28 [16]

In addition, Figure 4 intuitively exhibits relation curves of elastic constants with regard to applied pressure. In general, an elastic constant can be obtained by computing the elastic stiffness constants for second-order terms of the strain energy [32], while this work uses the stress–strain method to calculate elastic constant C_{ij} [33–35]. The results in Figure 4 indicate that C_{11}, C_{12}, and C_{44} gradually increase with an increase in applied pressure within the range of 0 GPa to 50 GPa. Additionally, C_{11} increases at the fastest rate. The stability criterion of expression (1) is satisfied by C_{11}, C_{12}, and C_{44}, which means that the FeTi alloy can remain stable under high pressure and the structural phase transition occurs with difficulty.

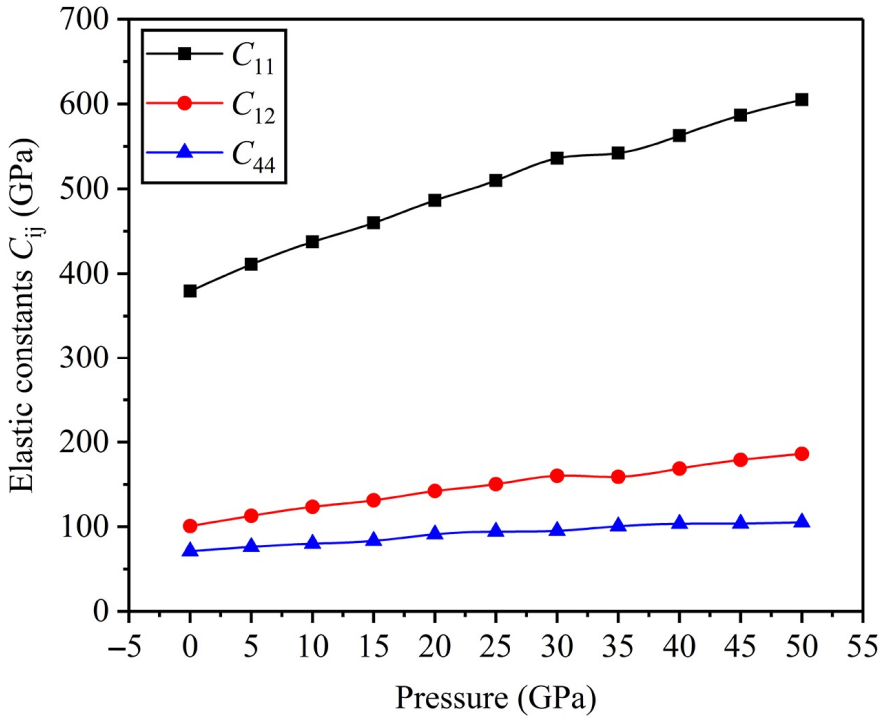


Figure 4. Relation curves of elastic constant C_{ij} versus applied pressure.

3.2. Mechanical Properties

Alloy materials are known for having many great mechanical properties, like excellent strength and plasticity; in general, these properties depend on the moduli of material, including shear modulus G, Young's modulus E, and bulk modulus B [36,37]. These parameters correspond to the ability to withstand material deformation, and the higher the moduli are, the less the material deforms. The moduli for the cubic polycrystalline materials are calculated using the following Formulas (2)–(4) using the Voigt–Reuss–Hill (VRH) method [38,39], and Table 2 shows the calculated moduli.

$$B = \frac{1}{3}(C_{11} + 2C_{12}) \tag{2}$$

$$G = \frac{1}{2}(G_V + G_R) \tag{3}$$

$$E = \frac{9BG}{3B + G} \tag{4}$$

In the above equations, G_V and G_R indicate the Voigt and Reuss shear modulus, respectively, and they are given by the following Equations (5) and (6):

$$G_V = \frac{(C_{11} - C_{12} + 3C_{44})}{5} \tag{5}$$

$$G_R = \frac{5(C_{11} - C_{12})C_{44}}{4C_{44} + 3(C_{11} - C_{12})} \tag{6}$$

Figure 5 shows variation curves of Young's modulus E, bulk modulus B, and shear modulus G versus applied pressure. From Figure 5, the results indicate that E, B, and G monotonically raise as applied pressure increases, suggesting that FeTi alloys have stronger resistance to the elastic, bulk, and shear deformation when applied pressure increases.

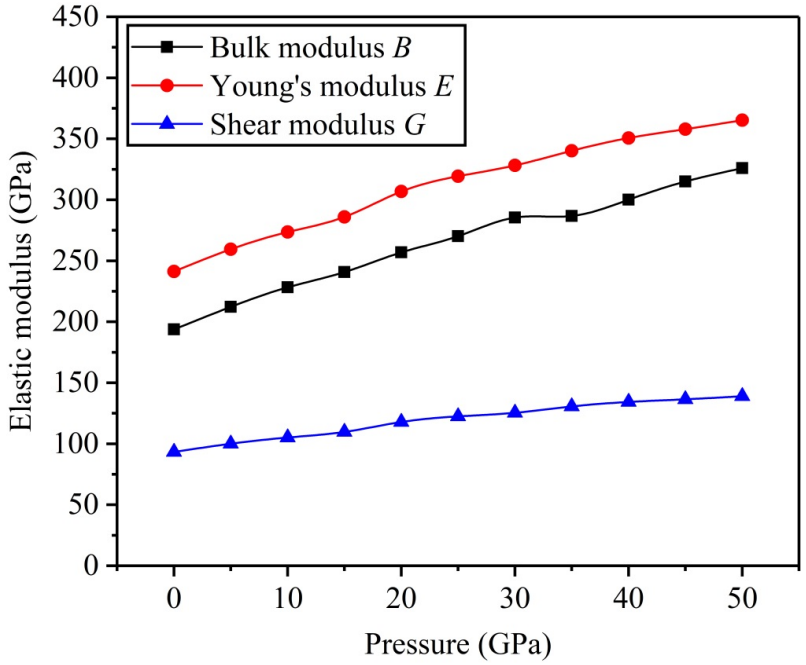


Figure 5. Relation curves of Young's modulus, bulk modulus, and shear modulus versus applied pressure.

Ductile-to-brittle transition occurs easily during material phase transition. For polycrystalline pure metals, Pugh et al. [37] revealed that the B/G ratio was used for assessing the ductile/brittle properties. In general, the critical value $B/G = 1.75$ is to distinguish brittle or ductile material. The material for $B/G < 1.75$ exhibits brittleness, and the material for $B/G > 1.75$ characterizes toughness, and a bigger B/G indicates better ductility, while a smaller B/G represents stronger brittleness, which is commonly applied for evaluating ductile/brittle transition in intermetallic compounds [40]. The results in Figure 6 show that the calculated B/G is approximately equal to 2.075 for $P = 0$ GPa, and B/G tends to increase as the applied pressure goes up, which means that the FeTi alloy is a kind of material with good ductility, and the ductility of the FeTi alloy is increased under high pressure.

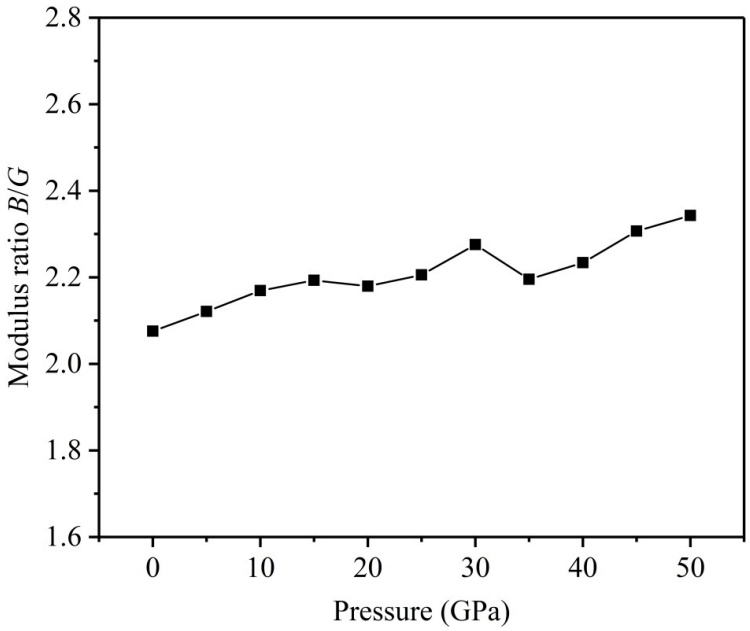


Figure 6. Relation curves of *B/G* versus applied pressure.

3.3. Anisotropy

Elastic anisotropy is a crucial physical parameter for studying mechanical properties of anisotropic materials, and elastic anisotropy is described by the anisotropy factor A. In isotropic materials, A is equal to a unit (i.e., A = 1), but A is unequal to a unit for anisotropic materials, and when A is greater or less than the value of the one, the materials exhibit stronger anisotropy [41,42]. In addition, Yoo [43] put forward the cross-slip-pinning model to study the relationships between anisotropy factor A and mechanical properties. A higher A induced a larger force to drive the motion of screw dislocation, which motivated the process of cross-slip-pinning. For a cubic FeTi alloy, the anisotropy factors are calculated as follows [44,45]:

$$A_{(100)[001]} = \frac{2C_{44}}{C_{11} - C_{12}} \tag{7}$$

$$A_{(110)[001]} = \frac{C_{44}(C' + 2C_{12} + C_{11})}{C_{11}C' - C_{12}^2} \tag{8}$$

Herein, $C' = (C_{11} + C_{12})/2 + C_{44}$, $A_{(100)[001]}$ and $A_{(110)[001]}$ denote the anisotropy factors in the directions of $(100)[001]$ and $(110)[001]$, respectively. Based on Equations (7) and (8), $A_{(100)[001]}$ and $A_{(110)[001]}$ are calculated at various pressures, as shown in Figure 7. The results in Figure 7 show that the initial characteristic of the FeTi alloy is anisotropic because of $A_{(100)[001]} = 0.51$ and $A_{(110)[001]} = 0.587$ at $P = 0$, and the two values do not change much when applied pressure increases, but they fluctuate between $P = 15$ GPa and $P = 45$ GPa and have a minimum value of $A_{(100)[001]} = 0.502$ and $A_{(110)[001]} = 0.579$ under $P = 50$ GPa, implying that the anisotropies are the strongest under $P = 50$ GPa in $(100)[001]$ and $(110)[001]$ directions and contribute to the movement of screw dislocation.

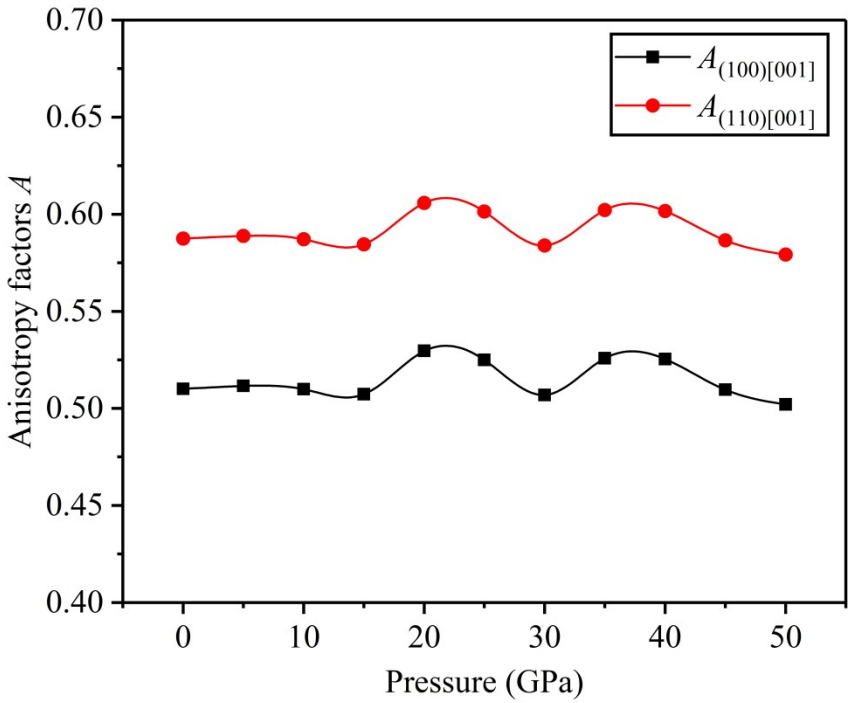


Figure 7. Relation curves of A versus applied pressure.

Poisson's ratio σ is considered as another crucial physical factor in studying the plasticity of materials, and the σ value is −1~0.5; a large σ value denotes good plasticity. Reed et al. [46] concluded that σ was between 0.25 and 0.5 in central force solids. Based on Equations (9) and (10) [44,47], $\sigma_{[001]}$ and $\sigma_{[111]}$ in the [001] and [111] directions are calculated at various pressures and plotted in Figure 8. The results show $\sigma_{[001]} = 0.21$ and $\sigma_{[111]} = 0.336$ under $P = 0$ GPa, which means that the central force is the main interatomic

bonding in the [001] and [111] directions. Additionally, $\sigma_{[001]}$ and $\sigma_{[111]}$ increase basically with the increase in applied pressure, but they fluctuate within the pressure range of $P = 20$ GPa to $P = 40$ GPa, and there is a maximum value at $P = 30$ GPa, which indicates better plasticity. Therefore, the plasticity of materials can be enhanced under high pressure in the directions of [001] and [111].

$$\sigma_{[001]} = \frac{C_{12}}{C_{11} + C_{12}} \tag{9}$$

$$\sigma_{[111]} = \frac{C_{11} + 2C_{12} - 2C_{44}}{2(C_{11} + 2C_{12} + C_{44})} \tag{10}$$

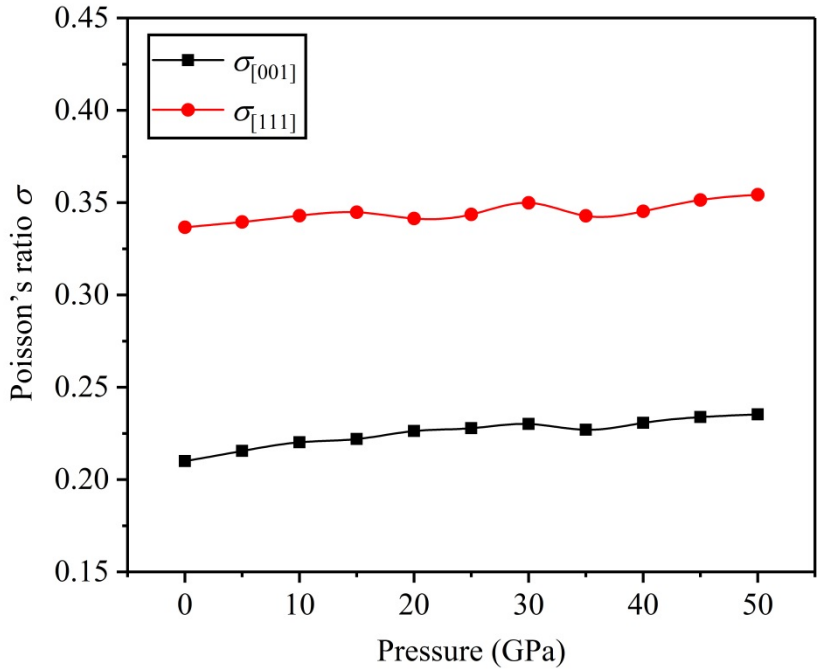


Figure 8. Relation curves of σ versus applied pressure.

For further study of the deformation resistance and mechanical properties of the FeTi alloy, $G_{(100)[010]}$, $G_{(110)[1\bar{1}0]}$, and $E_{\langle 100\rangle}$ are calculated, which denote the shear moduli in the $(100)[010]$ and $(110)[1\bar{1}0]$ directions, respectively, and they are obtained via $G_{(100)[010]} = C_{44}$ and $G_{(110)[1\bar{1}0]} = (C_{11} - C_{12})/2$, and $E_{\langle 100\rangle}$ is Young's modulus in the $\langle 100\rangle$ direction, expressed by $E_{\langle 100\rangle} = (C_{11} - C_{12})[1 + C_{12}/(C_{11} + C_{12})]$ [48,49]. In Figure 9, we plot the curves of elastic constants versus the applied pressure via the calculated data. The results show that $G_{(100)[010]}$ is smaller with regard to $G_{(110)[1\bar{1}0]}$ when the same pressure is applied, suggesting that the shear deformation in the $(110)[1\bar{1}0]$ direction is more difficult compared with the $(100)[010]$ direction under the same pressure. In addition, the value of $E_{\langle 100\rangle}$ gradually increases as pressure increases, implying that increasing pressure may prevent elastic deformation in the $\langle 100\rangle$ direction. For metals and compounds, Cauchy pressure $C_{12} - C_{14}$ is generally applied to characterize the angular properties of atomic bonding [50]. Cauchy pressure describes the nature of atomic bonding, and when the value is positive, the uniform electron gas surrounds all the spherical atoms and the local environment is considered to be the same in electron distribution, which implies the metallic characteristic with atomic bonding, while negative Cauchy pressure means that the atoms are bonded in a specific direction, and this directionality becomes stronger as the Cauchy pressure becomes more negative [49,51]. The result from Figure 9 indicates that Cauchy pressure remains positive under different pressures and gradually increases as

pressure increases, implying that metallic bond is predominant and gets stronger under high pressure.

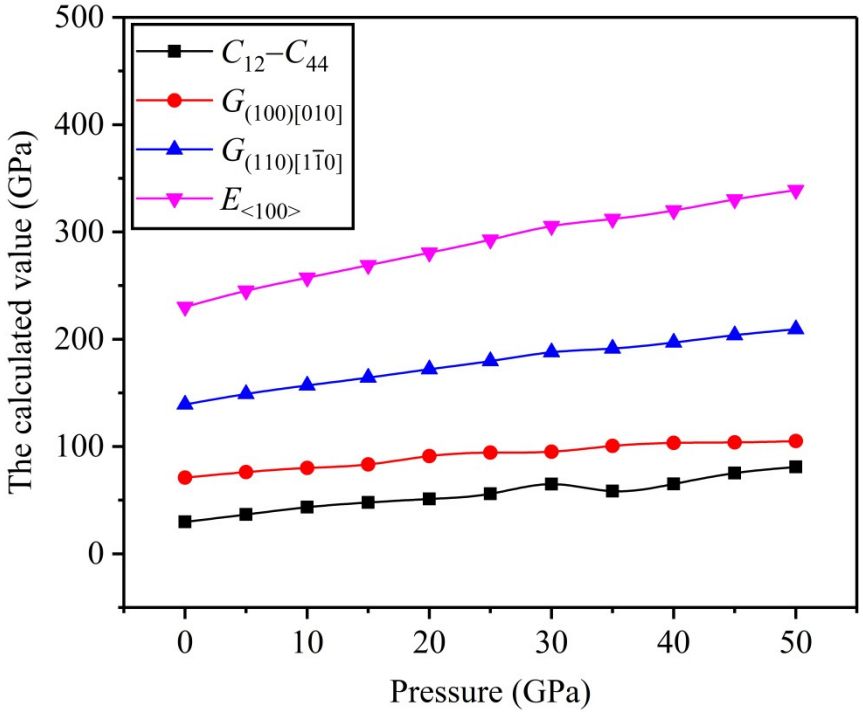


Figure 9. Relation curves of material modulus versus applied pressure.

3.4. Hardness and Yield Strength

In the process of investigating mechanical properties of materials, two vital properties, including hardness and yield strength, need be considered, which are defined as the abilities of materials to resist deformation [52]. According to the previous works [53–56], the modified Vickers hardness computational model was derived by Equation (11) for polycrystalline materials [57] and $k = G/B$. Equation (12) for calculating yield strength can be obtained via conventional empirical relation $H_V = 3\sigma_y$. Based on the calculated data, we plot the relation curves of the Vickers hardness and yield strength of the FeTi alloy versus applied pressure in Figure 10a,b. When the pressure is less than 25 GPa, H_V and σ_y increase as pressure increases and then decrease, and there is a maximum value at $P = 35$ GPa. When the pressure is greater than 35 GPa, the values of H_V and σ_y continue to decrease. However, the H_V and σ_y under high pressure are always larger than the value at $P = 0$ GPa, indicating that high pressure can enhance the Vickers hardness and yield strength of the FeTi hydrogen storage alloy.

$$H_v = 2\left(k^2 G\right)^{0.585} - 3 \tag{11}$$

$$\sigma_y = H_V/3 \tag{12}$$

3.5. Energy Factor K

The energy factor K is an important parameter in investigating the dislocation nucleation capacity and plastic properties for crystalline materials. Generally, we use elastic constants to calculate the energy factor K of dislocation in anisotropic materials. For cubic crystals, Equations (13) and (14) give the expressions of K factors of edge and screw dislocations [58,59]. From the calculated results, Figure 11 depicts the variation curves of K factors of edge and screw dislocations versus applied pressure. The results demonstrate that the K factors of edge and screw dislocations increase as pressure increases, thereby suggesting that high pressure inhibits the nucleations of screw and edge dislocations and

tends to reduce the plasticity of FeTi hydrogen storage alloys. In addition, the K_{edge} factor for edge dislocation is always larger with respect to screw dislocation, suggesting that edge dislocation is more difficult to nucleate with regard to screw dislocation.

$$K_{\text{screw}} = \left[\frac{1}{2}C_{44}(C_{11} - C_{12})\right]^{\frac{1}{2}} \tag{13}$$

$$K_{\text{edge}} = (C_{11} + C_{12})\left[\frac{(C_{11} - C_{12})C_{44}}{(C_{11} + C_{12} + 2C_{44})C_{11}}\right]^{\frac{1}{2}} \tag{14}$$

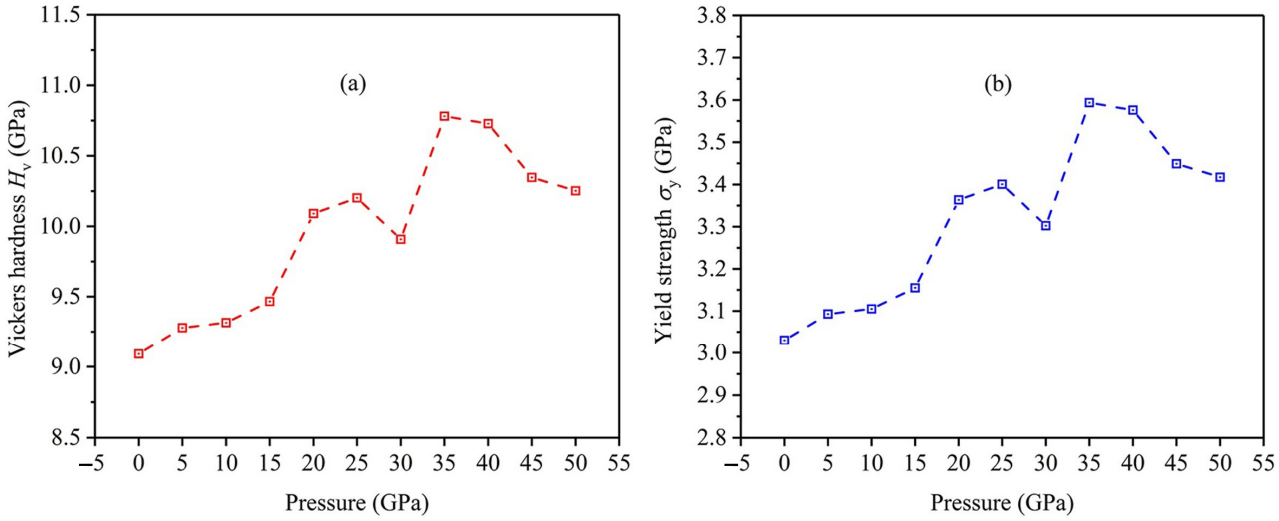


Figure 10. Relation curves of H_V (**a**) and σ_y (**b**) versus applied pressure.

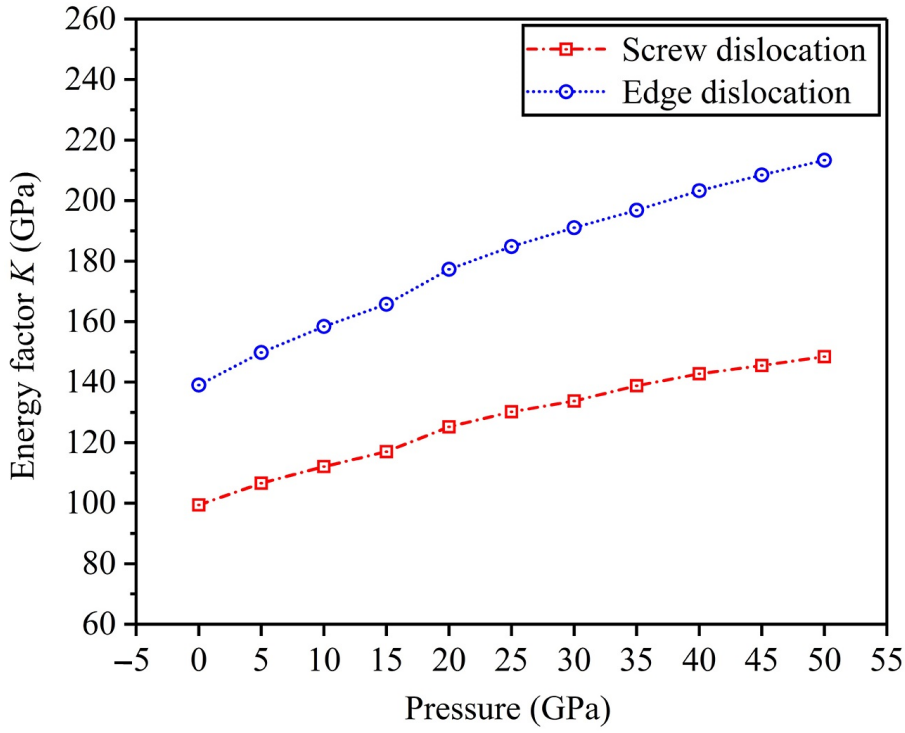


Figure 11. Relation curves of K factors for screw and edge dislocations versus applied pressure.

To further understand the dislocation properties of the FeTi alloy, relation curves of the K_{mixed} factor of mixed dislocation need to be investigated with regard to the direction

angle θ $(0 \leq \theta \leq \pi)$ according to Equations (15) and (16) [59,60]. Herein, the direction angle θ denotes the angle between the Burgers vector and the dislocation line. Based on the K_{mixed} factor, the dislocation width ζ is deduced as Equation (16), where d indicates the distance between neighboring slip planes and $C = (C_{11} - C_{12})/2$. Under different pressures, Figure 12a,b plot the relation curves of K_{mixed} factor and dislocation width ζ with regard to direction angle θ $(0 \leq \theta \leq \pi)$. The results demonstrate that the K_{mixed} factor increases as pressure increases for screw $(\theta = 0)$ and edge dislocation $(\theta = \pi/2)$ in Figure 12a. In addition, the nucleation of edge dislocation is more difficult due to the larger K_{edge} factor compared with screw dislocation, which consists with the conclusions of Figure 11. In Figure 12b, the dislocation widths ζ for screw $(\theta = 0)$ and edge dislocation $(\theta = \pi/2)$ decrease with the increase in the applied pressure. For edge dislocation $(\theta = \pi/2)$, the dislocation width is the minimum at $P = 50$ GPa, which results in maximum stacking-fault energy, thereby implying that high pressure suppresses twinning deformation and then reduces the plasticity of the FeTi hydrogen storage alloy.

$$K_{\text{mixed}} = K_{\text{edge}} \cdot \sin^2\theta + K_{\text{screw}} \cdot \cos^2\theta \tag{15}$$

$$\zeta = \frac{K_{\text{mixed}} \cdot d}{2C} \tag{16}$$

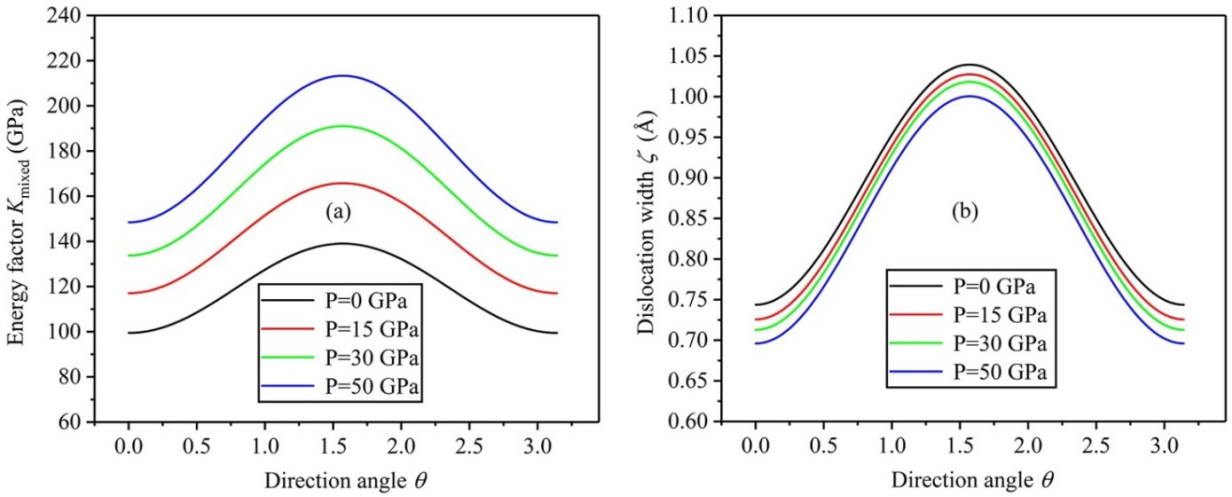


Figure 12. Relation curves of K_{mixed} factor for mixed dislocation (**a**) and dislocation width ζ (**b**) with regard to direction angle θ $(0 \leq \theta \leq \pi)$ under different pressures.

3.6. Electronic Properties

In the process of studying the bond mechanism of metals or alloys, the primary consideration is the electronic structure between atoms. We utilize it to describe the structural stability of the FeTi alloy at high pressure. To study the change in the total density of states (TDOS) at high pressure, Figure 13 plots the TDOS curves near the Fermi energy E_F under 0, 15, 25, 35, and 50 GPa pressures. The results demonstrate that with the increase in pressure, the energy of the valence-band top (VBT) decreases, but the energy of the conduction-band bottom (CBB) increases, which increases the difficulty of the electron jump from the VBT to the CBB, and the binding forces between atoms get stronger, suggesting that high pressure is inclined to promote the structural stability of the FeTi hydrogen storage alloy, instead of structural transition induced by high pressure.

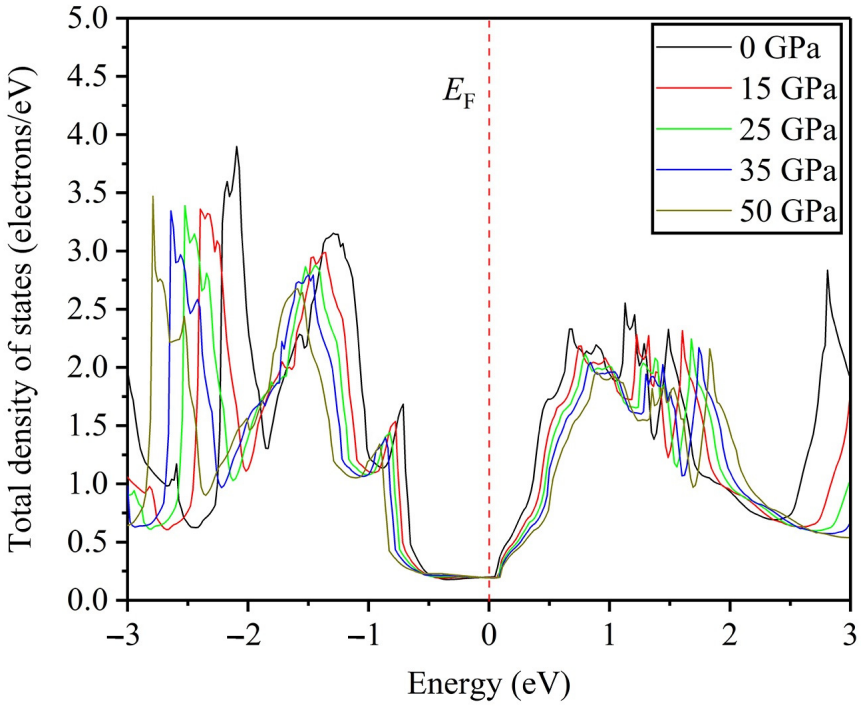


Figure 13. Total density of states for FeTi alloy at various pressures.

4. Conclusions

In summary, this study aimed to probe the influences of applied pressure on the structure, mechanics, dislocation, and electronics properties of an FeTi hydrogen storage alloy via first-principles calculations. The main conclusions are summarized as follows:

(1) In the range of applied pressure (0–50 GPa), an FeTi alloy can exist stably and is not prone to producing structural phase transition.

(2) With increasing pressure, the abilities to resist bulk and elastic deformations get stronger. An FeTi alloy is a kind of material with good ductility, and its ductility can be enhanced at high pressure.

(3) Shear deformation in the $(110)[1\bar{1}0]$ direction is more difficult than that in the $(100)[010]$ direction under the same pressure, and high pressure prevents elastic deformation in the $\langle 100 \rangle$ direction. Cauchy pressure indicates that the metallic bond is predominant and gets stronger under high pressure.

(4) High pressure can generally enhance the Vickers hardness and yield strength of an FeTi alloy, and the maximum values of Vickers hardness and yield strength occur at $P = 35$ GPa.

(5) High pressure inhibits dislocation nucleation and twinning deformation and then reduce the plasticity of FeTi hydrogen storage alloys. The edge dislocation is more difficult to nucleate with regard to screw dislocation.

(6) The TDOS reveals that high pressure is inclined to promote the structural stability for FeTi hydrogen storage alloys instead of structural transition induced by high pressure.

Author Contributions: Methodology, Formal Analysis, Investigation, Writing—Original Draft, L.Z. and Z.W.; Funding Acquisition, Supervision, Visualization, Z.W. and L.M.; Project Administration, Data Curation, H.C.; Software, P.T.; Writing—Review and Editing, Z.W. and L.M. All authors have read and agreed to the published version of the manuscript.

Funding: This research was funded by the National Natural Science Foundation of China (52162009), Natural Science Foundation of Hunan Province (2021JJ40035), and State Key Laboratory of Advanced Design and Manufacturing for Vehicle Body, Hunan University, Changsha, China (32175006).

Data Availability Statement: The data presented in this study are available on request from the corresponding author.

Conflicts of Interest: The authors declare no conflict of interest.

References

1. Abdin, Z.; Zafaranloo, A.; Rafiee, A.; Mérida, W.; Lipiński, W.; Khalilpour, K.R. Hydrogen as an energy vector. *Renew. Sustain. Energy Rev.* **2020**, *120*, 109620. [CrossRef]
2. Salmon, N.; Bañares-Alcántara, R. Green ammonia as a spatial energy vector: A review. *Sustain. Energy Fuels* **2021**, *5*, 2814–2839. [CrossRef]
3. Guilbert, D.; Vitale, G. Hydrogen as a Clean and Sustainable Energy Vector for Global Transition from Fossil-Based to Zero-Carbon. *Clean Technol.* **2021**, *3*, 881–909. [CrossRef]
4. Shang, Y.Y.; Liu, S.F.; Liang, Z.D.; Pyczak, F.; Lei, Z.F.; Heidenreich, T.; Schkel, A.; Kai, J.J.; Gizer, G.; Dornheim, M. Developing sustainable FeTi alloys for hydrogen storage by recycling. *Commun. Mater.* **2022**, *3*, 101. [CrossRef]
5. Padhee, S.P.; Roy, A.; Pati, S. Mechanistic insights into efficient reversible hydrogen storage in ferrotitanium. *Int. J. Hydrogen Energy* **2020**, *46*, 906–921. [CrossRef]
6. Niu, J.Z.; Guo, Y.H.; Li, K.; Liu, W.J.; Zhou, L. Improved mechanical, bio-corrosion properties and in vitro cell responses of Ti-Fe alloys as candidate dental implants. *Mater. Sci. Eng. C* **2021**, *122*, 111917. [CrossRef]
7. Liang, L.; Wang, F.; Rong, M.H.; Wang, Z.M.; Yang, S.T.; Wang, J.; Zhou, H.Y. Recent Advances on Preparation Method of Ti-Based Hydrogen Storage Alloy. *J. Mater. Sci. Chem. Eng.* **2020**, *8*, 18–38. [CrossRef]
8. Ko, W.S.; Park, K.B.; Park, H.K. Density functional theory study on the role of ternary alloying elements in TiFe-based hydrogen storage alloys. *J. Mater. Sci. Chem. Eng.* **2021**, *33*, 148–158. [CrossRef]
9. Liu, H.; Zhang, J.X.; Sun, P.; Zhou, C.S.; Liu, Y. An overview of TiFe alloys for hydrogen storage: Structure, processes, properties, and applications. *J. Energy Storage* **2023**, *68*, 107772. [CrossRef]
10. Dematteis, E.M.; Berti, N.; Cuevas, F.; Latroche, M.; Baricco, M. Substitutional effects in TiFe for hydrogen storage: A comprehensive review. *Mater. Adv.* **2021**, *2*, 2524–2560. [CrossRef]
11. Zhou, C.S.; Zhang, J.X.; Bowman, R.C.; Fang, Z.Z. Roles of Ti-Based Catalysts on Magnesium Hydride and Its Hydrogen Storage Properties. *Inorganics* **2021**, *9*, 36. [CrossRef]
12. Padhee, S.P.; Roy, A.; Pati, S. Role of Mn-substitution towards the enhanced hydrogen storage performance in FeTi. *Int. J. Hydrogen Energy* **2022**, *47*, 9357–9371. [CrossRef]
13. Alvares, E.; Jerabek, P.; Shang, Y.; Santhosh, A.; Pistidda, C.; Heo, T.W.; Sundman, B.; Dornheim, M. Modeling the thermodynamics of the FeTi hydrogenation under para-equilibrium: An ab-initio and experimental study. *Calphad* **2022**, *77*, 102426. [CrossRef]
14. Nong, Z.; Zhu, J.; Yang, X.; Cao, Y.; Lai, Z.; Liu, Y. First-principles study of hydrogen storage and diffusion in B2 FeTi alloy. *Comput. Mater. Sci.* **2014**, *81*, 517–523. [CrossRef]
15. Benyelloul, K.; Bouhadda, Y.; Bououdina, M.; Faraoun, H.I.; Aourag, H.; Seddik, L. The effect of hydrogen on the mechanical properties of FeTi for hydrogen storage applications. *Int. J. Hydrogen Energy* **2014**, *39*, 12667–12675. [CrossRef]
16. Zhu, L.F.; Friák, M.; Udyansky, A.; Ma, D.; Neugebauer, J. Ab initio based study of finite-temperature structural, elastic and thermodynamic properties of FeTi. *Intermetallics* **2014**, *45*, 11–17. [CrossRef]
17. Kresse, G.; Furthmüller, J. Efficient iterative schemes for ab initio total-energy calculations using a plane-wave basis set. *Phys. Rev. B* **1996**, *54*, 11169–11186. [CrossRef]
18. Kresse, G.; Hafner, J. Ab initio molecular dynamics for liquid metals. *Phys. Rev. B* **1993**, *47*, 558–561. [CrossRef]
19. Blöchl, P.E. Projected augmented-wave method. *Phys. Rev. B* **1994**, *50*, 17953–17979. [CrossRef]
20. Perdew, J.P.; Burke, K.; Ernzerhof, M. Generalized gradient approximation made simple. *Phys. Rev. Lett.* **1996**, *77*, 3865–3868. [CrossRef]
21. Pack, J.D.; Monkhorst, H.J. Special Points for Brillonin-Zone Integrations. *Phys. Rev. B* **1976**, *13*, 5188.
22. Birch, F. Finite elastic strain of cubic crystals. *Phys. Rev.* **1947**, *71*, 809. [CrossRef]
23. Lv, P.; Peng, C.; Liu, Q.Y.; Zhong, C.L.; Huang, D.F.; Liu, Z.C.; Zhou, Q.B.; Zhao, R.X. Effect of regulating the different proportions of Zr to Mn elements on the hydrogen storage properties of titanium–iron–manganese–hydrogen storage alloys. *RSC Adv.* **2023**, *13*, 10157–10167. [CrossRef] [PubMed]
24. Park, K.B.; Fadonougbo, J.O.; Park, C.S.; Lee, J.H.; Na, T.K.; Kang, H.S.; Ko, W.S.; Park, H.K. Effect of Fe substitution on first hydrogenation kinetics of TiFe-based hydrogen storage alloys after air exposure. *Int. J. Hydrogen Energy* **2021**, *46*, 30780–30789. [CrossRef]
25. Nong, Z.; Zhu, J.; Yu, H.; Lai, Z. First principles calculation of intermetallic compounds in FeTiCoNiVCrMnCuAl system high entropy alloy. *Trans. Nonferrous Met. Soc.* **2012**, *22*, 1437–1444. [CrossRef]
26. Patil, S.K.R.; Khare, S.V.; Tuttle, B.R.; Bording, J.K.; Kodambaka, S. Mechanical stability of possible structures of PtN investigated using first-principles calculations. *Phys. Rev. B* **2006**, *73*, 104118. [CrossRef]
27. Wang, J.; Yip, S.; Phillpot, S.R.; Wolf, D. Crystal instabilities at finite strain. *Phys. Rev. Lett.* **1993**, *71*, 4182. [CrossRef]
28. Wallace, D.C. Thermodynamics of Crystals. *Am. J. Phys.* **1972**, *40*, 1718. [CrossRef]

29. Buchenau, U.; Schober, H.R.; Welter, J.M.; Arnold, G.; Wagner, R. Lattice dynamics of $Fe_{0.5}Ti_{0.5}$. *Phys. Rev. B* **1983**, *27*, 955–962. [CrossRef]
30. Liebertz, J.; Stähr, S.; Haussühl, S. Growth and properties of single crystals of FeTi. *Krist. Tech.* **1980**, *15*, 1257–1260. [CrossRef]
31. Cheng, D.; Zhao, S.; Wang, S.; Ye, H. First-principles study of the elastic properties and electronic structure of NiTi, CoTi and FeTi. *Philos. Mag. A* **2001**, *81*, 1625–1632. [CrossRef]
32. Souissi, M.; Numakura, H. Elastic properties of Fe–C and Fe–N martensites. *ISIJ Int.* **2015**, *55*, 1512–1521. [CrossRef]
33. Shang, S.L.; Wang, Y.; Liu, Z.K.; Ye, H. First-principles elastic constants of α- and θ-Al_2O_3. *Appl. Phys. Lett.* **2007**, *90*, 101909. [CrossRef]
34. Ganeshan, S.; Shang, S.L.; Zhang, H.; Wang, Y.; Mantina, M.; Liu, Z.K. Elastic constants of binary Mg compounds from first-principles calculations. *Intermetallics* **2009**, *17*, 313–318. [CrossRef]
35. Boucetta, S. Theoretical study of elastic, mechanical and thermodynamic properties of MgRh intermetallic compound. *J. Magnes. Alloy* **2014**, *2*, 59–63. [CrossRef]
36. Yang, X.W.; Zhu, J.C.; Lai, Z.H.; Liu, Y.; He, D.; Nong, Z.S. Finite element analysis of quenching temperature field, residual stress and distortion in A357 aluminum alloy large complicated thin-wall workpieces. *Trans. Nonferrous Met. Soc.* **2013**, *23*, 1751–1760. [CrossRef]
37. Lu, Y.; Yang, Y.; Zheng, F.; Wang, B.T.; Zhang, P. Electronic, mechanical, and thermodynamic properties of americium dioxide. *J. Nucl. Mater.* **2013**, *441*, 411–420. [CrossRef]
38. Hill, R. The elastic behavior of crystalline aggregate. *Proc. Phys. Soc. A* **1952**, *65*, 349–354. [CrossRef]
39. Iotova, D.; Kioussis, N.; Lim, S.P. Electronic structure and elastic properties of the Ni3X (X=Mn, Al, Ga, Si, Ge) intermetallics. *Phys. Rev. B* **1996**, *54*, 14413–14422. [CrossRef] [PubMed]
40. Cottrel, A.H. Advanced Structural Materials. In Proceedings of the European Conference on Advanced Materials and Processes, Cambridge, UK, 22–24 July 1991.
41. Fu, H.; Li, D.; Peng, F.; Gao, T.; Cheng, X. Structural and elastic properties of γTiAl under high pressure from electronic structure calculations. *J. Alloys Compd.* **2009**, *473*, 255–261. [CrossRef]
42. Mattesini, M.; Ahuja, R.; Johansson, B. Cubic Hf_3N_4 and Zr_3N_4: A class of hard materials. *Phys. Rev. B* **2003**, *68*, 184108. [CrossRef]
43. Yoo, M.H. On the theory of anomalous yield behavior of Ni_3Al—Effect of elastic anisotropy. *Scr. Metall.* **1986**, *20*, 915–920. [CrossRef]
44. Fu, H.; Li, X.F.; Liu, W.F.; Ma, Y.; Tao, G.; Hong, X. Electronic and dynamical properties of NiAl studied from first principles. *Intermetallics* **2011**, *19*, 1959–1967. [CrossRef]
45. Lau, K.; McCurdy, A.K. Elastic anisotropy factors for orthorhombic, tetragonal, and hexagonal crystals. *Phys. Rev. B* **1998**, *58*, 8980–8984. [CrossRef]
46. Reed, R.P.; Clark, A.F. *Materials at Low Temperatures*; American Society for Metals: Russell, OH, USA, 1983.
47. Friák, M.; Šob, M.; Vitek, V. Ab initio calculation of tensile strength in iron. *Philos. Mag.* **2003**, *83*, 3529–3537. [CrossRef]
48. Fu, H.; Peng, W.; Gao, T. Structural and elastic properties of ZrC under high pressure. *Mater. Chem. Phys.* **2009**, *115*, 789–794. [CrossRef]
49. Fu, H.; Li, D.; Peng, F.; Gao, T.; Cheng, X. Ab initio calculations of elastic constants and thermodynamic properties of NiAl under high pressures. *Comput. Mater. Sci.* **2008**, *44*, 774–778. [CrossRef]
50. Pettifor, D.G. Theoretical predictions of structure and related properties of intermetallics. *Mater. Sci. Tech.* **1992**, *8*, 345–349. [CrossRef]
51. Johnson, R.A. Analytic nearest-neighbor model for fcc metals. *Phys. Rev. B* **1988**, *37*, 3924–3931. [CrossRef]
52. Tse, J.S. Intrinsic hardness of crystalline solids. *J. Superhard Mater.* **2010**, *32*, 177–191. [CrossRef]
53. Smedskjaer, M.M.; Mauro, J.C.; Yue, Y. Prediction of glass hardness using temperature-dependent constraint theory. *Phys. Rev. Lett.* **2010**, *105*, 115503. [CrossRef] [PubMed]
54. Li, K.; Wang, X.; Zhang, F.; Xue, D. Electronegativity identification of novel superhard materials. *Phys. Rev. Lett.* **2008**, *100*, 235504. [CrossRef] [PubMed]
55. Gao, F.; He, J.; Wu, E.; Liu, S.; Yu, D.; Li, D.; Zhang, S.; Tian, Y. Hardness of covalent crystals. *Phys. Rev. Lett.* **2003**, *91*, 015502. [CrossRef] [PubMed]
56. Šimůnek, A.; Vackář, J. Hardness of Covalent and Ionic Crystals: First-Principle Calculations. *Phys. Rev. Lett.* **2006**, *96*, 085501. [CrossRef] [PubMed]
57. Chen, X.; Niu, H.; Li, D.; Li, Y. Modeling hardness of polycrystalline materials and bulk metallic glasses. *Intermetallics* **2011**, *19*, 1275–1281. [CrossRef]
58. Savin, M.M.; Chernov, V.M.; Strokova, A.M. Energy factor of dislocations in hexagonal crystals. *Phys. Status Solidi A* **1976**, *35*, 747–754. [CrossRef]
59. Foreman, A.J.E. Dislocation energies in anisotropic crystals. *Acta Metall.* **1955**, *3*, 322–330. [CrossRef]
60. Reid, C.N. Dislocation widths in anisotropic B.C.C. crystals. *Acta Metall.* **1966**, *14*, 13–16. [CrossRef]

Disclaimer/Publisher's Note: The statements, opinions and data contained in all publications are solely those of the individual author(s) and contributor(s) and not of MDPI and/or the editor(s). MDPI and/or the editor(s) disclaim responsibility for any injury to people or property resulting from any ideas, methods, instructions or products referred to in the content.